An ALE Based Hybrid Meshfree Local RBF-Cartesian FD Scheme for Incompressible Flow around Moving Boundaries

A. Javed[1], K. Djidjeli[2], Jing T. Xing[3] and Z. Sun[4]
Faculty of Engineering and Environment, University of Southampton, SO171BJ, UK

A solution scheme is presented to simulate incompressible viscous flow around moving boundaries using hybrid meshfree-Cartesian grid. The presented solution approach avoids intensive re-meshing and enhances computational efficiency by combining the advantages of both meshfree and mesh-based methods for flow around moving objects. The scheme employs a body conformal meshfree nodal cloud around the solid object which convects with the moving solid boundary. On the outer side, meshfree nodal cloud is surrounded and partially overlapped by a stationary Cartesian grid. Navier Strokes equations in Arbitrary-Lagrangian-Eulerian (ALE) formulations are solved over moving nodal cloud using meshfree local Radial Basis Functions in finite difference Mode (RBF-FD). Eulerian form of flow equations are solved over static Cartesian grid using conventional finite difference scheme. Meshfree nodes can efficiently adapt to the moving boundary without necessitating re-meshing. Use of finite difference method over Cartesian grid allows faster computing and improves computational efficiency. Variation in computation time has been studied with corresponding change in size of meshfree and Cartesian grids. Significant reduction in computation time is achieved by reducing the size of meshfree cloud. The solution scheme is validated by simulating two dimensional flows around vibrating cylindrical objects. For this purpose, forced as well as vortex induced cylindrical vibration cases are investigated and solutions are compared with computational and experimental results available in literature.

Nomenclature

ϕ	=	radial basis function
r	=	radial distance
σ	=	RBF shape parameter
P	=	pressure
$\vec{u}$	=	flow velocity
$\vec{v}$	=	velocity of grid point
∂_t	=	time derivative
Re	=	Reynolds number
∇	=	gradient operator
t	=	time
Ω	=	boundary
$\boldsymbol{n}$	=	outward normal direction to boundary
x,y	=	Cartesian coordinates
$\|\|.\|\|$	=	standard Euclidean norm
$\mathcal{L}$	=	differential operator
w	=	RBF weight
ρ	=	flow density
μ	=	dynamic viscosity

[1] CED Group, Faculty of Engineering and Environment, University of Southampton, SO171BJ, UK.
[2] CED Group, Faculty of Engineering and Environment, University of Southampton, SO171BJ, UK.
[3] FSI Group, Faculty of Engineering and Environment, University of Southampton, SO171BJ, UK.
[4] CED Group, Engineering and Environment, University of Southampton, SO171BJ, UK.

ν = kinematic viscosity
D = Diameter of cylinder
U = free stream velocity
C_L = coefficient of lift
C_D = coefficient of drag
f = frequency of solid vibration
f_s = Strouhal frequency
F = frequency ratio
St = Strouhal number
Y = vibration amplitude
$y(t)$ = vertical displacement at time t
m = mass of cylinder
k = spring stiffness
k^*_{eff} = effective elasticity

Subscripts
j,k = node (particle) number

Superscript
n = Number of time iteration

I. Introduction

TRADITIONAL mesh-based methods (Finite Element, Finite Volume, and Finite Difference) have widely been practiced for solving flow problems since the advent of Computational Fluid Dynamics (CFD). These methods have therefore evolved as well-developed and robust flow simulation techniques and are commercially employed worldwide. However, requirement of mesh (or grid), in these methods, imposes a pre-defined connectivity constraint amongst the nodes which strongly limits their utilization for problems involving moving boundaries and complex geometries.

Over past two decades, meshfree methods have emerged as a class of promising computational techniques which can effectively overcome the limitations experienced by traditional mesh-based methods. Meshfree methods do not suffer from limitations associated grid connectivity. Without the constraints of grid, nodes can be moved, added or removed from domain more flexibly during the simulation process. Meshfree methods are therefore, considered to be a better choice for problems involving complex geometries, moving boundaries, large deformation and adaptive refinement. However, these methods suffer from reduced computational efficiency compared with their mesh-based counterparts. This is due to the requirement of increased number of neighboring particles to achieve required order of accuracy [1]. Therefore, the bandwidth of the matrices, representing the sets of algebraic equations increases. As a result, more computational resources are required to proceed with the solution. Moreover, calculation of shape / kernel functions, in meshfree methods, also increases the computational cost. On the contrary grid-based methods are low on computational resources and allow faster computing. Nevertheless, meshfree methods can effectively negotiate with moving boundaries without necessitating frequent re-meshing and are therefore better suited for flow around moving objects.

Radial Basis Functions (RBFs) have historically been used for multidimensional interpolation over scattered data points. In early 90s, Kansa [2] proposed the use of RBFs for solution of Partial Differential Equation (PDEs) over scattered data points. Later, the researchers effectively applied RBFs, for global collocation in the evolving meshfree techniques [3-7]. Global RBFs however showed inaccuracies arising from ill-conditioned coefficient matrices, when dealing with large number of data points. The problem was later resolved by the use of local RBFs [1, 8, 9] which produce well-conditioned, sparse matrices to efficiently deal with non-linearities [10].

RBF in Finite Difference Mode (RBF-FD) is a local RBF method which was independently proposed by Tolstykh et al [8] and Wright et al [1] for different set of applications. Local RBFs have been shown to be highly efficient in solving flow problem [9-13]. However, like other meshfree methods, RBF based methods are no exception to the limitation of high computational cost.

Recently, Hybrid grid techniques have been used to deal with flow problems over moving boundaries. These methods attempt to limit the use of computationally expensive meshfree methods by coupling these with mesh-based methods. Ding et al [14] presented a hybrid FD/MLSFD method for solving the 2-D Navier Strokes equations in

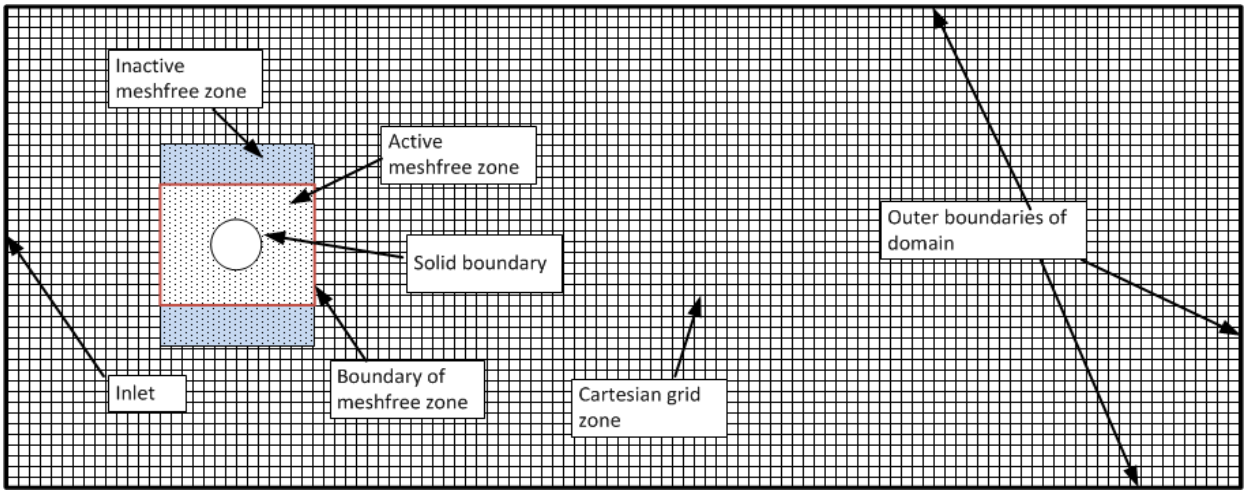

Figure 1. Schematic of Hybrid meshfree / meshed domain

streamfunction-vorticity formulation. A Meshfree grid was generated around solid body and embedded over a non-body conformal background Cartesian grid. Later, Chew et al [15] extended similar scheme for moving bodies by using ALE based formulation. Fries and Matthies [16] developed a stabilized solver for incompressible N-S equations by coupling meshfree Galerkin methods with mesh based finite element method. Javed et al. [17] proposed a coupled local RBF-FD scheme over meshfree zone and conventional Finite Difference (FD) scheme on meshed zone for flow around arbitrarily shaped stationary objects. The scheme used a body conformal meshfree zone which was surrounded by Cartesian grid. Finite difference scheme was used over Cartesian mesh to achieve computational efficiency. The use of meshfree technique was limited to small meshfree zone around the solid object where it could efficiently deal with complex geometries in bargain of high computational cost.

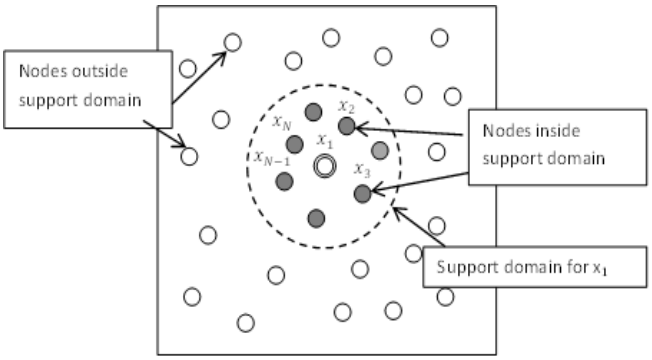

Figure 2. Support Domain of a Reference Node in RBF-FD

Here, a coupled meshfree and mesh-based solution scheme is presented for incompressible, viscous Navier Strokes equations in pressure-velocity formulation over a hybrid grid to efficiently deal with flow around moving boundaries. For this purpose, a body conformal meshfree nodal cloud is generated around moving solid object. Meshfree nodes move and morph along with the solid body and are able to efficiently adapt to the moving boundaries. Movement of nodes is accounted for by using Arbitrary-Lagrangian-Eulerian (ALE) formulation of N-S

Table 1. Commonly used Radial Basis Functions

Type of Basis Function	Expression for $\phi(r)$
Multiquadric (MQ)	$\phi(r) = \sqrt{r^2 + \sigma^2}$
Inverse Multiquadric (IMQ)	$\phi(r) = 1/\sqrt{r^2 + \sigma^2}$
Inverse Quadric (IQ)	$\phi(r) = 1/(r^2 + \sigma^2)$
Gaussian (GA)	$\phi(r) = \exp(-(\sigma r)^2)$

equation in Meshfree zone. ALE approach provides an elegant way of solving the equations over moving nodes (or grid points) by combining the features of Eulerian as well as Lagrangian approaches. A stationary Cartesian grid surrounds and partially overlaps the meshfree cloud. The meshfree nodes falling in overlapping zone are treated as 'inactive' and do not participate in the computation process. These inactive meshfree nodes however, become active when they appear from behind the Cartesian zone during the movement of meshfree cloud. The detailed description of this mechanism is presented in section-II (B). Eulerian framework is applied over stationary Cartesian mesh to deal with N-S equations. Spatial discretization of governing flow Equations is achieved using Local Radial Basis Functions in Finite Difference Mode (RBF-FD) over meshfree nodes. Conventional 5-point central differencing is used for space splitting on Cartesian grid. Non-incremental pressure update fractional step scheme[18] is used for time discretization of N-S equations in the entire domain. Use of meshfree cloud allows the flexibility to deal with arbitrary shaped objects. Schematic of the proposed coupled approach is shown in Fig. 1. Meshfree nodes can also adapt to the moving boundaries without necessitating frequent re-meshing. On the other hand, Cartesian grid ensures faster computing by using conventional Finite difference scheme. The method thus benefits from the strengths of both meshfree and meshed approaches.

II. Problem Formulation

A. Governing Equations

Non-dimensionalized, incompressible, transient, viscous Navier-Strokes equations in Arbitrary-Lagrangian-Eulerian (ALE) and pressure-velocity $(P, \vec{u})$ form are expressed as [19]:

$$\nabla.\vec{u} = 0 \tag{1}$$

$$\partial_t \vec{u} = -\nabla P - (\vec{u} - \vec{v})(\nabla.\vec{u}) + \left(\frac{1}{Re}\right)\nabla^2\vec{u} \tag{2}$$

For stationary Cartesian grid, $\vec{v}$ is set as zero resulting in Eulerian form of N-S equations. Pressure-velocity decoupling of momentum Eq. (1) is realized by fractional step scheme used by Kim and Moin [18]. It is a non-incremental pressure update procedure which does not contain pressure term in the decoupled momentum equation for intermediate velocity $\vec{u}^*$. The convective term of momentum Eq. (2) is treated with 2nd order explicit Adam-Bashforth scheme whereas viscous term is decomposed using 2nd order implicit Crank-Nicholson scheme [18]. The momentum equation can therefore, be split in the following manner:

$$\begin{aligned}(\vec{u}^* - \vec{u}^n)/\Delta t = -1/2[3(\vec{u}^n - \vec{v}^n)(\nabla.\vec{u}^n) - (\vec{u}^{n-1} - \vec{v}^{n-1})(\nabla.\vec{u}^{n-1})] \\ + 1/(2Re)[\nabla^2(\vec{u}^n + \vec{u}^*)]\end{aligned} \tag{3}$$

$$(\vec{u}^{n+1} - \vec{u}^*)/\partial t = -\nabla P^{n+1} \tag{4}$$

Applying divergence operator to Eq. (4) and enforcing continuity constraint (from Eq. (1)) on $\vec{u}^{n+1}$:

$$\nabla^2 P^{n+1} = (1/\Delta t)\nabla.\vec{u}^* \tag{5}$$

At every iteration, momentum Eq. (3) for intermediate velocity field is implicitly solved to get the nodal values of $\vec{u}^*$ subject to following condition on the boundary $\partial\Omega$:

$$\vec{u}^*|_{\partial\Omega} = (u^{n+1} + \Delta t \nabla P^n)_{\partial\Omega} \tag{6}$$

Intermediate velocity field is then used to evaluate the value of P^{n+1} by solving Eq. (5). Velocity values at next time step $\vec{u}^{n+1}$ are calculated using Eq. (4) subject to velocity boundary conditions

$$\vec{u}^{n+1}|_{\partial\Omega} = \vec{u}_{\partial\Omega} \tag{7}$$

Discretization of spatial derivatives appearing in Eq. (3) - (6), for nodes falling in meshfree zone, is achieved using local RBF in finite difference Mode. RBF-FD is the generalization of conventional finite difference over scatted data points [10]. The scheme suggests setting up an RBF interpolation problem at each meshfree node, say x_1, for every spatial derivative $\mathcal{L}$, using location of neighbouring nodes (or particles) $x_j \epsilon \mathbb{R}^d,\ j = 1,2, \ldots N$, in the local support domain, as shown in Fig. 2. Subsequently, RBF-FD weights ($w_{(1,j)}^{(\mathcal{L})}$) are calculated x_1, corresponding to all neighbouring points. RBF-FD approximation of differential operator $\mathcal{L}$ of a field variable u then is given by weighted linear sum of values of same variable at the neighbouring nodes [20]:

$$\mathcal{L}u(x_1) = \sum_{\mathrm{j=1}}^{\mathrm{N}} \mathrm{w}_{(1,\mathrm{j})}^{(\mathcal{L})}\, u(x_j) \tag{8}$$

Further detail of theory and formulation of RBF-FD can be found in literature [1, 8]. Some commonly used radial basis functions are shown in Table 1. Multiquadric (MQ) RBFs are used here. A time implicit scheme proposed by Javed et al. [12] is then used to solve the resulting system of equations at each time step.

Classical 5-point finite difference stencil is used to approximate 2-D spatial derivatives over Cartesian grid. Separate matrix equations are formulated for governing equations at respective meshfree and Cartesian zones. Local RBF, as well as 5-point central difference scheme yield sparse matrix equations which are solved using Generalized Minimum Residual (GMRES) method [21]. Solution of these equations, subject to boundary conditions, yields velocity and pressure values at every time iteration.

B. Treatment of Computational Domain

Configuration of meshfree and Cartesian zones has been shown in Fig. 1 for flow around moving objects. Body conformal meshfree nodal cloud surrounds the solid. Rectangular (or square) shape of outer periphery of meshfree cloud enables it to communicate effectively with Cartesian grid. All the meshfree nodes exactly follow the motion of the solid objects. Therefore the arrangement of computational nodes, around the moving boundary, does not change over time. On the outer side, meshfree cloud is surrounded and partially overlapped by the Cartesian grid. The meshfree nodes 'overshadowed' by Cartesian grid are treated as 'inactive' and do not participate in the computation process. When the meshfree cloud moves along with solid object, some of the meshfree nodes will hide behind the stationary Cartesian grid and become 'inactive'. At the same time, some meshfree nodes, on the other side of meshfree cloud, will appear from behind the overlapping region and will become 'active' to participate in the subsequent computation process. Pressure and velocity values are assigned to the 'newly born' nodes by approximating these values from surround nodes. These approximations can be worked out through a variety of interpolation techniques. RBF based interpolation is used here. Data available at active nodes falling in the support

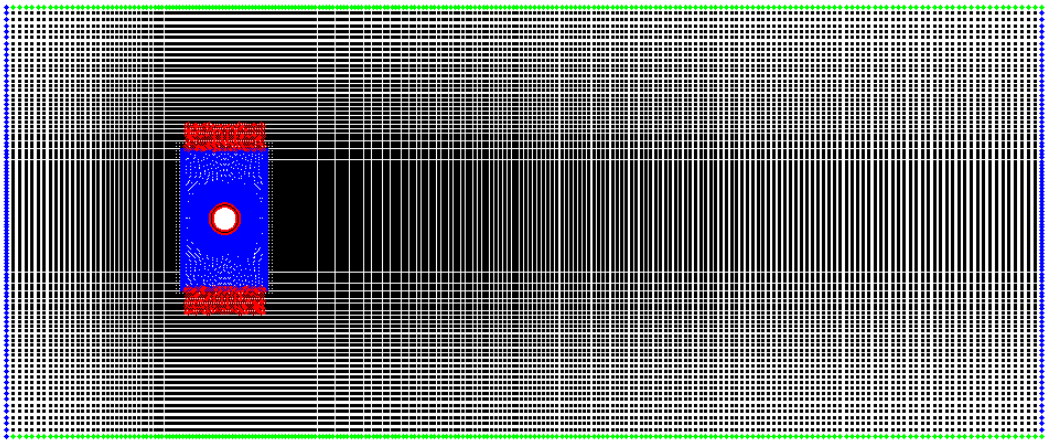

Figure 3. Hybrid Grid around cylinder

domain of newly born node is used for interpolation.

The hybrid grid generated around cylindrical objects is shown in Fig. 3. Nodes are arranged radially around cylinder in meshfree zone. Radial displacement of nodes gradually increases as they move away from the cylinder. Cartesian grid around meshfree zone also refines gradually while going close to the cylinder. A closed in view in Fig. 4 shows nodal arrangement in meshfree zone and Cartesian grid around it.

For the purpose of calculation, computational nodes have been divided into five different categories. Category-I is assigned to those of nodes of Cartesian grid which are at a reasonable distance from meshfree zone. Cartesian nodes which are expected to fall within the influence domain of some of the meshfree nodes due to proximity of meshfree zone are called Category-II nodes. Results at these nodes may influence the results of corresponding meshfree nodes. Category-III, IV and V are meshfree nodes. Category-III nodes fall exactly at the outer boundary of active meshfree zone. These nodes also act as boundary nodes for Cartesian grid. Category-IV nodes fall inside the active meshfree zone. Category-V nodes are the meshfree nodes which are superimposed by Cartesian grid. These nodes are inactive and do not participate in calculation. Nodes in Category-I and II are part of 'fixed' Cartesian grid and are therefore kept stationary during simulation. Moreover, as Category-III nodes have to act as boundary nodes for stationary Cartesian grid; these nodes are also kept fixed so that they can effectively communicate with Cartesian Grid. Category-IV and V nodes however, move with the solid boundary.

By using RBF-FD scheme in meshfree zone and 5-point central differencing scheme in Cartesian Zone, separate systems of equations are formulated for each zone. Each system is independently solved at each time step. Cartesian and meshfree zones communicates with each other by influencing the other zone through their Category-II or Category-III nodes respectively.

Process of activation and deactivation of meshfree nodes, as they move with the boundary during the simulation, is shown in Fig. 4. During upward motion of the cylindrical object, some of the nodes, near the upper edge of meshfree zone, move into Cartesian region and hide behind it. At the same time, 'inactive' nodes near the lower edge of active meshfree zone appear from behind the Cartesian zone and become active. Field variables at these nodes are assigned values by interpolating results from surrounding nodes. It is pertinent to note that the nodes at the boundary of active meshfree zone are not moving with the solid objects (though they are the part of meshfree zone). This feature makes sure that boundary nodes for Cartesian grid remain fixed and unchanged irrespective of the motion of meshfree zone.

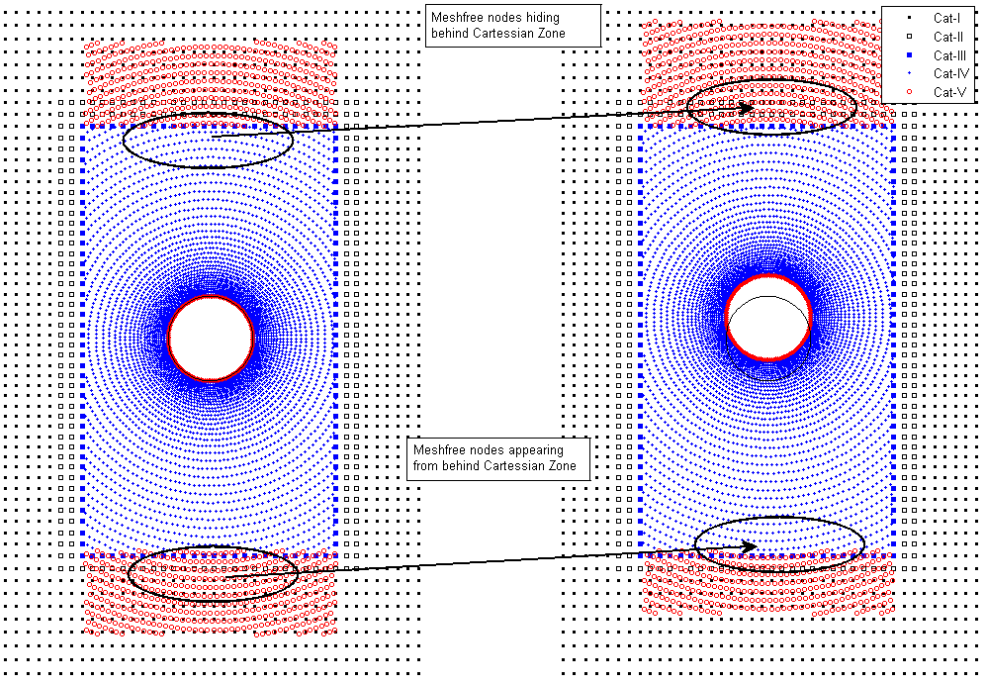

Figure 4. Activation and Deactivation of meshfree nodes during motion of nodal cloud along with the Solid

During this process, position and number of Cartesian nodes remains unchanged. This results in computational advantage as the coefficient matrices representing Eqs. (3) and (5) in Cartesian zone remain unchanged. Therefore, coefficient matrices representing equations in only meshfree zone need to be updated. In view of the fact, that Cartesian zone constitutes larger portion of the entire computational domain, significant computational time is saved using this approach.

C. Computational Algorithm

Following is the detail of computational process:

1) At the start of simulation process, RBF-FD weights are calculated for all active meshfree nodes (Cat-III and IV nodes) at the start of simulation. Subsequently, coefficient matrices of Eq. (3) and (5) are formulated for meshfree and Cartesian zones separately.
2) Intermediate momentum Eq. (3) is solved to calculate Intermediate velocity values ($\vec{u}^*$) in meshfree zone. Boundary conditions defined in Eq. (6) are used.
3) Pressure (P^{n+1}) in meshfree zone is then calculated by solving Eq. (5). Pressure boundary conditions are derived from Eq. (4). Subsequently, velocity values for next time iteration ($\vec{u}^{n+1}$) are calculated using Eq. (4).
4) Similarly, Eqs. (3), (4) and (5) are solved for nodes in Cartesian zone. The spatial derivatives are obtained using five point central difference scheme. Velocity and pressure values on Cat-III nodes are used as boundary conditions for Cartesian nodes next to active meshfree zone.
5) New position of moving boundary is worked out for current simulation time. For forced vibration case, the displacement-time equation of the moving body is used to calculate the position of boundary. For vortex induced vibration case, aerodynamic forces are calculated over the solid boundary using fluid pressure and velocity profiles. Equation of motion for the solid is then solved using explicit Runge-Kutta method to get the displacement value.
6) Solid object along with the body conformal meshfree cloud are displaced to their new positions.
7) Category of Cat-IV and Cat-V nodes is updated based on their new locations. If there are any 'fresh' nodes in Cat-III, they are assigned pressure and velocity values by RBF interpolation of the values on the surrounding nodes.
8) RBF-FD weights are recalculated for all fresh nodes as well as for those meshfree nodes, the influence domains of which extend outside the active meshfree zone. Recalculation of RBF-FD Weights of these nodes is necessitated due to changed relative positions with respect to static nodes.
9) Coefficient matrices are reformulated, in meshfree zone, according new RBF-FD weights.

III. Numerical Tests

The coupled meshfree-mesh based solver has been tested for performance and accuracy by simulating flow problems around cylindrical objects. Computational performance has been tested for stationary cylinder case. Other test cases include flow around stationary cylinder at various Reynolds numbers and flow around vibrating cylinder. Non-stationary cylinder cases include forced vertical vibration as well as vortex induced vertical vibration. The detailed descriptions are outlined in the following subsections.

A. Computational Performance Test

It is understood that meshfree methods are computationally more intensive due to several reasons which include expensive calculation of weights or kernels (often necessitating square root and matrix inversion operations) and requirement of larger number of neighboring particles to ensure required order of accuracy [1]. Larger number of neighboring particles results denser coefficient matrices which require more number of calculation operations to be solved [22].

The numerical experiment is performed to study the variation in computational time with changing size of meshfree zone. For this purpose, flow problem is solved around static cylinder using hybrid meshfree-Cartesian approach. Computational domain is rectangular in shape. Size of the domain is *16D X 32D*. For performance test case only, cylinder is centered vertically as well as horizontally with the rectangular domain to allow larger variation in size of meshfree zone.

Flow problem is solved at Reynolds number 100. Reynolds number is calculated as $Re = \rho UD/\mu$. Free stream velocity boundary condition ($\vec{u} = (U, 0)$) is applied at the inlet. No slip boundary conditions have been introduced at the solid boundary Ω_D ($\vec{u}|_{\Omega_D} = \vec{v}_D$). Along top and bottom boundaries vertical derivative of velocity is assumed

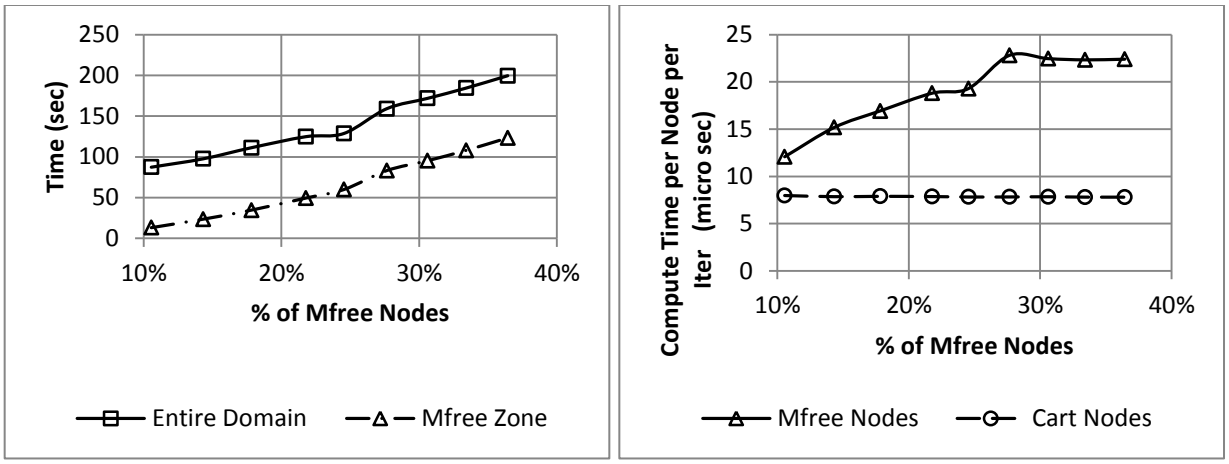

(a) **(b)**

Figure 5. Computational performance with changing size of meshfree zone. a) Total and meshfree computation time with increasing percentage of meshfree nodes in computational domain. b) Average computation time per node per iteration for meshfree and Cartesian zones

zero ($\partial\vec{u}/\partial\boldsymbol{n} = 0$). At the outlet boundary Ω_o, the so called 'do-nothing' boundary conditions are applied to ensure smooth propagation of wake. This boundary condition dictates $-(p - p_{ref})\boldsymbol{n} + \nu\partial\vec{u}/\partial\boldsymbol{n} = 0$, where p_{ref} is the reference pressure.

Computation time of first 500 iterations has been noted for different sizes of meshfree domain. Various sizes of active meshfree zone are tested ranging from *2D X 2D* (containing 2116 nodes) to *6D X 6D* (containing 11011 nodes). Changing the size of meshfree zone therefore varied the percentage number of meshfree nodes in the entire computational domain. Variation of computation time with changing percentage of meshfree nodes is shown in Fig. 5 (a). Increasing the proportion of meshfree nodes from 10.5% to 36.5% actually increased the computational cost by 2.3 times. During this change, computation time of meshfree solver also increased by almost 9.5 times. Increase in computation time is caused by increasing orders of coefficient matrices which happen to be more resource intensive during solution process. A plot of average computation time by each node in a single iteration is shown in Fig. 5 (b). Enlarging the meshfree zone increases average computational time by each meshfree node. On the contrary, average computation time of Cartesian nodes stays constant and significantly lower than their meshfree counterparts. Therefore, computationally efficient configuration would entail smaller sized meshfree zone in the entire domain.

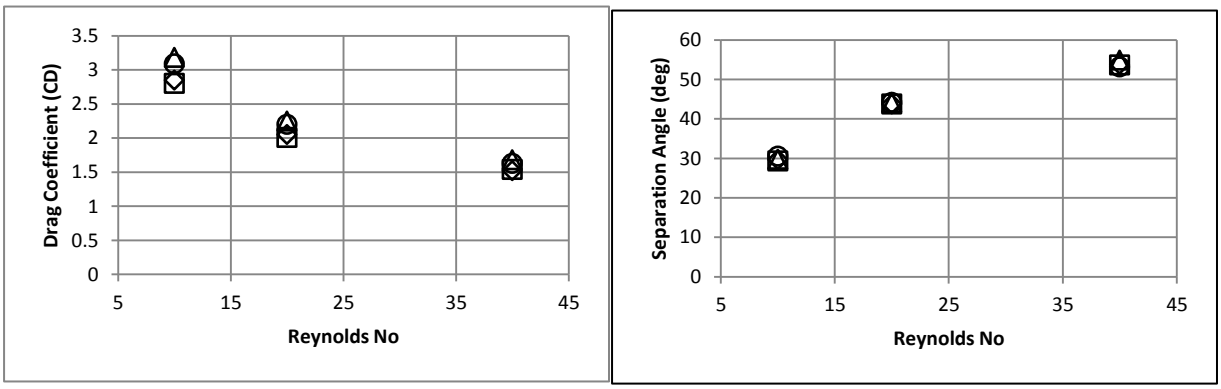

(a) **(b)**

Figure 6. Results for steady flow cases around stationary cylinder (◊ Dennis and Chang [26], □ Takami and Keller[25], Δ Tuann and Olson [27], ○ Present work). a) Drag Coefficient Vs Re . b) Separation angle Vs Re

B. Fixed Boundary Test Case

Flow problems around stationary cylinder have been solved at Reynolds Numbers 10, 20, 40, 100 and 200. It is well known that, at low Reynolds number (Re<49), flow leaves the cylinder in a steady manner. However between Reynolds numbers 49 to 200, the flow becomes unsteady and forms oscillating vortices (so called Kamran vortices) downstream the cylinder. These type of flow problems have extensively been studied [14, 23-27] and their results are well established. The tests are therefore often simulated to validate newly presented numerical solution schemes.

A rectangular domain of size *16DX38D* is chosen for this problem. Cylinder is placed vertically in the middle of the domain and at a distance of *16D* from inlet and *30D* from outlet. This ensures that the flow near the solid is not affected by the boundary conditions at outer domain boundaries. The size of meshfree zone is *3DX3D*. Therefore, active meshfree zone constitutes only 1.48% of the total domain size. A radial grid is generated in meshfree zone around cylinder. Number of nodes at cylindrical surface is 150. There are total of 26799 nodes in the entire domain out of which 4959 nodes fall in meshfree zone. Boundary conditions are the same as mentioned in Section III-B. Time step is kept as $5\text{x}10^{-3}$ sec for steady flow cases and $2.5\text{x}10^{-3}$ for unsteady cases. Lift and drag coefficients are calculated using following expressions:

$$C_L = \frac{Lift}{\rho U^2 D} \tag{9}$$

$$C_D = \frac{Drag}{\rho U^2 D} \tag{10}$$

For steady flow cases (Re = 10, 20, 40), lift coefficient remains zero. However, resultant values of drag coefficients and separation angle are calculated and compared with solutions from previous researches [25-27] in Fig. 6. For Reynolds number 100 and 200, oscillating vortex also causes fluctuation in lift and drag profiles over time. As a result, lift coefficient oscillate around zero and drag coefficient fluctuate around a non-zero mean value. Frequency of wake oscillation can be characterized by Strouhal frequency which is the frequency of lift force oscillation. Strouhal number is then calculated using following equation:

$$St = f_s \frac{D}{U} \tag{11}$$

For unsteady flow cases (Re=100 and 200), resultant values of maximum lift coefficient (C_{Lmax}), mean drag coefficients (C_{Dmean}) and Strauhal numbers are compared with previous solutions [14, 23, 24] in Fig. 7. The results are found to be in good agreement with previous studies.

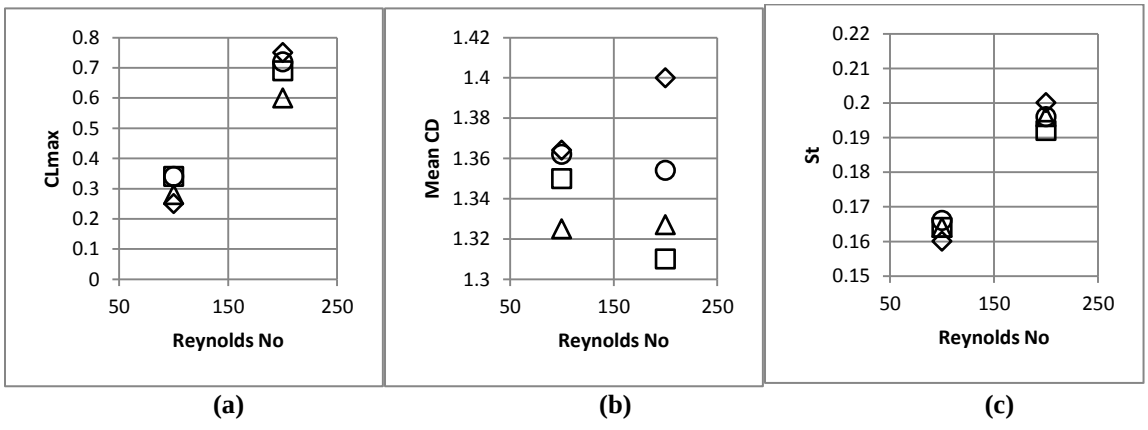

(a) **(b)** **(c)**

Figure 7. Results for unsteady flow cases around stationary cylinder (◊ Braza et al. [23], □ Liu et al. [24], Δ Ding et al. [14], ○ Present work). a) C_{Lmax} Vs *Re.* b) Mean C_D angle Vs *Re.* c) *St* Vs *Re*

C. Forced Vibration Case

Test cases are run for flow around cylinder which is forced to vibrate vertically with sinusoidal displacement profile over time. Vertical displacement of the solid about its mean position is expressed as:

$$y(t) = Y \sin(2\pi f t) \qquad (12)$$

In order to allow cylindrical oscillation, length of meshfree zone along vertical axis is extended. Therefore, the size of meshfree zone around the cylinder is kept as *3DX5D* for this case. Flow Reynolds number is set as 100. As mentioned before, period vortices are generated at this Reynolds number. Therefore, problem is often characterized by frequency ratio $F = f/f_s$. Computations are performed at an amplitude *Y=0.25D* and range of forced frequencies (f).

An important characteristic of these test cases is the presence of 'lock-in' zone which is defined as the domain of frequency ratios (*F*) and displacement amplitudes (*Y*), where vortex shedding frequency deviates from its original value and becomes equal to forced frequency [28]. Bounds of lock-in region on (*Y,F*) plane, defined experimentally by Koopman [29], at Re 100, at shown in Fig. 8. Results from present simulations are also shown on the same plot and agree well with experimental data [29]. Screenshots of vorticity profile of the flow (*Y=0.25D, F=0.50*) at various time intervals are shown in Fig. 9.

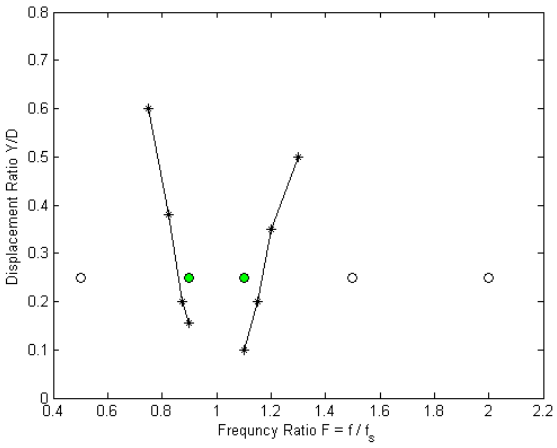

Figure 8. Bounds of Lock-in zone at Re 100 (* Experimental data [29], ○Unlocked results in present work, ● Lock-in results in present work)

Presence of lock-in zone is identified by spectral analysis of time profile of lift coefficient. Time profiles of lift coefficients and their power spectral density (PSD) plots, for locked-in configurations, are shown in Fig. 10. As vortex frequency equalizes with frequency of forced oscillation, therefore Lift-time curves are purely sinusoidal and PSD plots show single peaks. On the contrary, in unlocked configuration, vortex shedding frequency retains its identity. As a results, lift fluctuation profiles over time deviate from their pure sinusoidal behavior [30] due to presence of multiple frequencies. PSD plot also shows two distinct peaks at frequencies f and f_s. The results for unlocked configurations are shown in Fig. 11. Non-sinusoidal response of lift curves on time plots and separate peaks of forced as well as vortex shedding frequency on PSD plots are clearly visible.

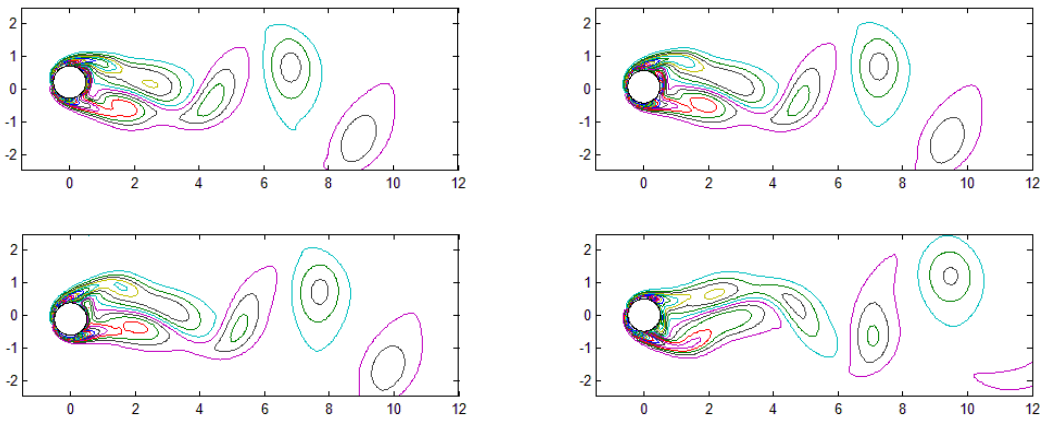

Figure 9. Vorticity profile around vibrating cylinder at Re100 (*Y=0.25D, F=1.50*)

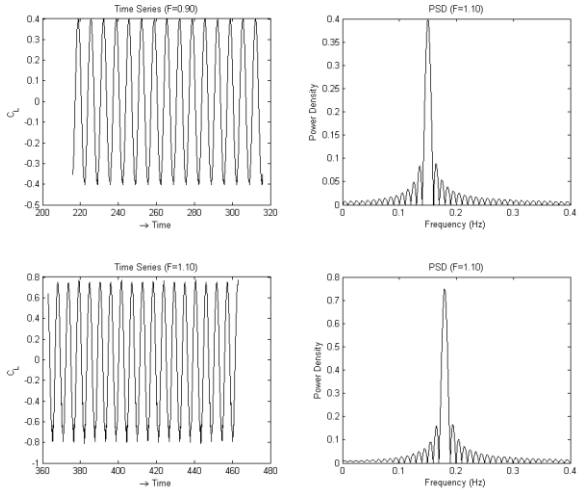

Figure 10. Time series of C_L and PSD plots (Lock-in configurations)

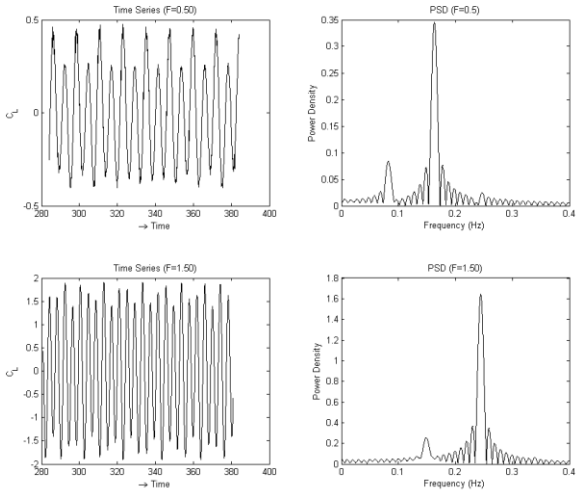

Figure 11. Time series of C_L and PSD plots (Unlocked configurations)

D. Vortex Induced Vibration Case

Flow around spring mounted cylinder is solved to simulate vortex induced vibration. Presence of spring provides single Degree of Freedom (DoF) to the system by allowing the cylinder to vibrate vertically. Schematic of the problem is shown in Fig. 12. Vortices shedding downstream the cylinder produce time oscillating lift profile around cylinder. These forces induce vibratory motion in the spring mounted cylinder. The phenomenon has been characterized as 'self-limiting' by Mittal and Kumar [31]. This means that vibration amplitudes are restrained by inherent system parameters. The factors limiting the vibration amplitudes include reduction in lift force and appearance of additional frequencies in the oscillation profiles of aerodynamic forces [30]. Solid vibration is governed by following equation:

$$m\ddot{y} + ky = Lift \tag{13}$$

All parameters are used in their non-dimensionalized form in above equation. System response can be better expressed by defining a parameter called 'effective elasticity' $\left(k_{eff}^{*}\right)$ which represents the unified effect of inertia and stiffness. Effective stiffness is expressed as [32]:

$$k_{eff}^{*} = k - 4\pi^2 m f^{*2} \tag{14}$$

In above equation f^{*} represents the non-dimensional reduced frequency defined as $f^{*} = fU/D$. Here, a set of simulations are performed at *Re* 100. Lift force values obtained from fluid solver are plugged in Eq. (13). Runge-Kutta-4 Method is used to solve Eq. (13) to get the solid displacement about mean its position. Cases are studied by changing spring stiffness k. Mass value is set as 3.3. Vortex shedding at various time instances is shown in Fig. 13. Resultant vibrational amplitudes and frequencies are plotted against corresponding effective elasticity $\left(k_{eff}^{*}\right)$ values and compared with the results of Shiels et al [32] as shown in Fig. 14 (a) and (b) respectively. The vibration amplitudes are found to be significantly high for $0 \leq k_{eff}^{*} \leq 4.0$. In high amplitude zone, vibration frequency deviates from vortex shedding frequency and equalizes with the natural frequency of the cylinder (see Fig. 14 (b)) resulting in large amplitudes. This zone is therefore called 'lock-in' zone. The amplitudes sharply reduce when effective elasticity is increased or decreased beyond this range.

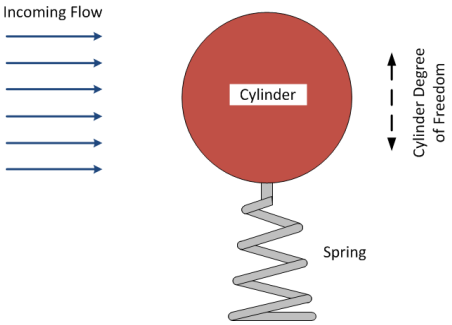

Figure 12. Schematic of flow induced vibration

IV. Conclusion

Current work aims to circumvent the performance related limitations of meshfree methods by restricting their use to the locations where these methods can supersede their mesh-based counterparts due to alleviation of nodal connectivity constraints. Presented scheme works well for both stationary and moving boundary cases. Phenomenon of locking-in was accurately predicted during forced and vortex induced vibration cases. Resultant amplitudes and frequencies of solid vibration were found in good agreement with previous solutions. Significant reduction in computational time can be achieved by limiting the size of meshfree zone in the domain. However, the size of active and inactive meshfree zone should still be large enough to allow the movement of solid boundary. In case of multiple moving bodies, separate nodal clouds can also be formed around each moving body. For multiple degrees of freedom systems, dimensions of meshfree zone may accordingly be adjusted to accommodate movement of boundary in more than one direction.

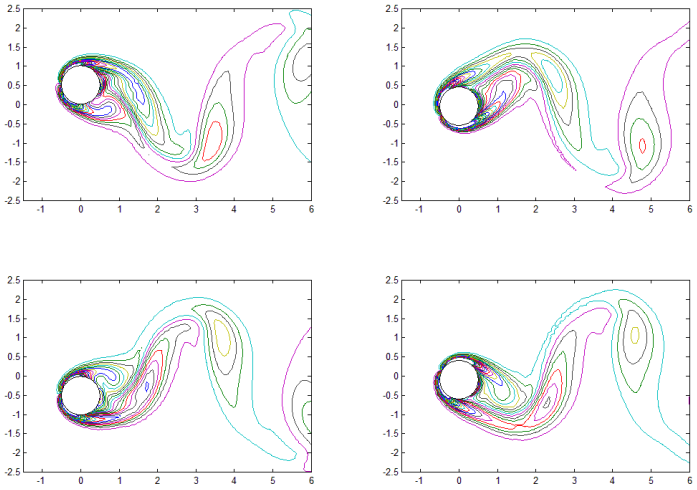

Figure 13. Vortex shedding behind cylinder for VIV case (m=3.3, k=5)

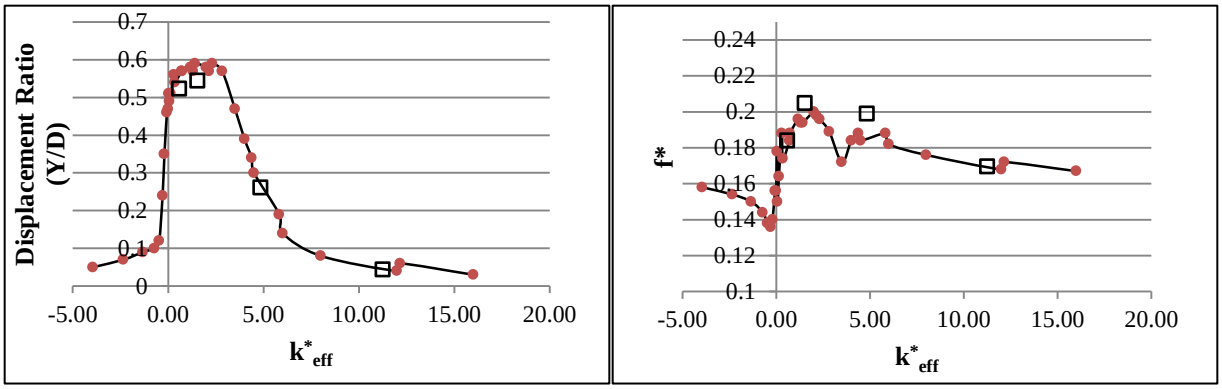

Figure 14. Result of vortex induced vibration test cases (● Shiels et al. [32], □ Present work). a) Displacement ratio Vs effective stiffness. b) Non-dimensionlized frequency Vs effective stiffness

References

[1] Wright, G. B., and Fornberg, B. "Scattered node compact finite difference-type formulas generated from radial basis functions," *Journal of Computational Physics* Vol. 212, No. 1, 2006, pp. 99-123.
doi: DOI 10.1016/j.jcp.2005.05.030

[2] Kansa, E. J. "Multiquadrics - a Scattered Data Approximation Scheme with Applications to Computational Fluid-Dynamics .2. Solutions to Parabolic, Hyperbolic and Elliptic Partial-Differential Equations," *Computers & Mathematics with Applications* Vol. 19, No. 8-9, 1990, pp. 147-161.
doi: Doi 10.1016/0898-1221(90)90271-K

[3] Franke, C., and Schaback, R. "Solving partial differential equations by collocation using radial basis functions," *Applied Mathematics and Computation* Vol. 93, No. 1, 1998, pp. 73-82.
doi: 10.1016/s0096-3003(97)10104-7

[4] Wang, J., and Liu, G. "Radial point interpolation method for elastoplastic problems," *ICSSD 2000: 1 st Structural Conference on Structural Stability and Dynamics*. 2000, pp. 703-708.

[5] Mai-Duy, N., and Tran-Cong, T. "Numerical solution of differential equations using multiquadric radial basis function networks," *Neural Networks* Vol. 14, No. 2, 2001, pp. 185-199.
doi: Doi 10.1016/S0893-6080(00)00095-2

[6] Liu, G. R., Yan, L., Wang, J. G., and Gu, Y. T. "Point interpolation method based on local residual formulation using radial basis functions," *Structural Engineering and Mechanics* Vol. 14, No. 6, 2002, pp. 713-732.

[7] Ling, L. V., and Kansa, E. J. "A least-square preconditioning for radial basis functions collocation methods," *Advances in Computational Mathematics* Vol. 23, 2005, pp. 31-54.

[8] Tolstykh, A. I., and Shirobokov, D. A. "On using radial basis functions in a "finite difference mode" with applications to elasticity problems," *Computational Mechanics* Vol. 33, No. 1, 2003, pp. 68-79.
doi: DOI 10.1007/s00466-003-0501-9

[9] Shu, C., Ding, H., and Yeo, K. S. "Local radial basis function-based differential quadrature method and its application to solve two-dimensional incompressible Navier-Stokes equations," *Computer Methods in Applied Mechanics and Engineering* Vol. 192, No. 7-8, 2003, pp. 941-954.
doi: Pii S0045-7825(02)00618-7
Doi 10.1016/S0045-7825(02)00618-7

[10] Chinchapatnam, P. P., Djidjeli, K., and Nair, P. B. "Radial basis function meshless method for the steady incompressible Navier–Stokes equations," *International Journal of Computer Mathematics* Vol. 84, No. 10, 2007, pp. 1509-1521.
doi: 10.1080/00207160701308309

[11] Shu, C., Ding., H., and Yeo., K. S. "Computation of Incompressible Navier-Stokes Equations by Local RBF-based Differential Quadrature Method," *Computer Modeling in Engineering and Sciences* Vol. 7, No. 2, 2005, pp. 195-206.

[12] Javed, A., Djijdeli, K., and Xing, J. T. "Shape adaptive RBF-FD implicit scheme for incompressible viscous Navier–Strokes equations," *Computers & Fluids* Vol. 89, No. 0, 2014, pp. 38-52.
doi: http://dx.doi.org/10.1016/j.compfluid.2013.10.028

[13] Javed, A., Djidjeli, K., and Xing, J. T. "Adaptive Shape Parameter (ASP) Technique for Local Radial Basis Functions (RBFs) and Their Application for Solution of Navier Strokes Equations," *International Conference on Fluids and Thermal Engineering*. International Scientific Council, Rome, Italy, 2013.

[14] Ding, H., Shu, C., Yeo, K. S., and Xu, D. "Simulation of incompressible viscous flows past a circular cylinder by hybrid FD scheme and meshless least square-based finite difference method," *Computer Methods in Applied Mechanics and Engineering* Vol. 193, No. 9-11, 2004, pp. 727-744.
doi: DOI 10.1016/j.cma.2003.11.002

[15] Chew, C. S., Yeo, K. S., and Shu, C. "A generalized finite-difference (GFD) ALE scheme for incompressible flows around moving solid bodies on hybrid meshfree–Cartesian grids," *Journal of Computational Physics* Vol. 218, No. 2, 2006, pp. 510-548.
doi: http://dx.doi.org/10.1016/j.jcp.2006.02.025

[16] Fries, T.-P., and Matthies, H. G. "A stabilized and coupled meshfree/meshbased method for the incompressible Navier–Stokes equations—Part II: Coupling," *Computer Methods in Applied Mechanics and Engineering* Vol. 195, No. 44–47, 2006, pp. 6191-6204.
doi: http://dx.doi.org/10.1016/j.cma.2005.12.003

[17] Javed, A., Djidjeli, K., Xing, J. T., and Cox, S. "A Hybrid meshfree local RBF- Cartesian FD scheme for incompressible flow around solid bodies," *International Conference on Fluid Mechanics and Applications*. International Scientific Council, Paris, France, 2013.

[18] Kim, J., and Moin, P. "Application of a Fractional-Step Method to Incompressible Navier-Stokes Equations," *Journal of Computational Physics* Vol. 59, No. 2, 1985, pp. 308-323.
doi: Doi 10.1016/0021-9991(85)90148-2

[19] Takashi, N., and Hughes, T. J. R. "An arbitrary Lagrangian-Eulerian finite element method for interaction of fluid and a rigid body," *Computer Methods in Applied Mechanics and Engineering* Vol. 95, No. 1, 1992, pp. 115-138.
doi: 10.1016/0045-7825(92)90085-X

[20] Chinchapatnam, P. P., Djidjeli, K., Nair, P. B., and Tan, M. "A compact RBF-FD based meshless method for the incompressible Navier-Stokes equations," *Proceedings of the Institution of Mechanical Engineers Part M-Journal of Engineering for the Maritime Environment* Vol. 223, No. M3, 2009, pp. 275-290.
doi: Doi 10.1243/14750902jeme151

[21] Saad, Y., and Schultz, M. H. "GMRES: A generalized minimal residual algorithm for solving nonsymmetric linear systems," *SIAM Journal on scientific and statistical computing* Vol. 7, No. 3, 1986, pp. 856-869.

[22] Fornberg, B., and Lehto, E. "Stabilization of RBF-generated finite difference methods for convective PDEs," *Journal of Computational Physics* Vol. 230, No. 6, 2011, pp. 2270-2285.
doi: http://dx.doi.org/10.1016/j.jcp.2010.12.014

[23] Braza, M., Chassaing, P., and Minh, H. H. "Numerical Study and Physical Analysis of the Pressure and Velocity-Fields in the near Wake of a Circular-Cylinder," *Journal of Fluid Mechanics* Vol. 165, 1986, pp. 79-130.
doi: Doi 10.1017/S0022112086003014

[24] Liu, C., Zheng, X., and Sung, C. "Preconditioned multigrid methods for unsteady incompressible flows," *Journal of Computational Physics* Vol. 139, No. 1, 1998, pp. 35-57.

[25] Takami, H., and Keller, H. B. "Steady Two-Dimensional Viscous Flow of an Incompressible Fluid past a Circular Cylinder," *Physics of Fluids* Vol. 12, No. 12, 1969, pp. II-51-II-56.

[26] Dennis, S., and Chang, G.-Z. "Numerical solutions for steady flow past a circular cylinder at Reynolds numbers up to 100," *J. Fluid Mech* Vol. 42, No. 3, 1970, pp. 471-489.

[27] Tuann, S.-y., and Olson, M. D. "Numerical studies of the flow around a circular cylinder by a finite element method," *Computers & Fluids* Vol. 6, No. 4, 1978, pp. 219-240.
doi: http://dx.doi.org/10.1016/0045-7930(78)90015-4

[28] Nobari, M. R. H., and Naderan, H. "A numerical study of flow past a cylinder with cross flow and inline oscillation," *Computers & Fluids* Vol. 35, No. 4, 2006, pp. 393-415.
doi: http://dx.doi.org/10.1016/j.compfluid.2005.02.004

[29] Koopmann, G. "The vortex wakes of vibrating cylinders at low Reynolds numbers," *Journal of Fluid Mechanics* Vol. 28, No. 03, 1967, pp. 501-512.

[30] Placzek, A., Sigrist, J.-F., and Hamdouni, A. "Numerical simulation of an oscillating cylinder in a cross-flow at low Reynolds number: Forced and free oscillations," *Computers & Fluids* Vol. 38, No. 1, 2009, pp. 80-100.
doi: http://dx.doi.org/10.1016/j.compfluid.2008.01.007

[31] Mittal, S., and Kumar, V. "Flow-induced vibrations of a light circular cylinder at Reynolds numbers 10 3 to 10 4," *Journal of Sound and Vibration* Vol. 245, No. 5, 2001, pp. 923-946.

[32] Shiels, D., Leonard, A., and Roshko, A. "Flow-induced vibration of a circular cylinder at limiting structural parameters," *Journal of Fluids and Structures* Vol. 15, No. 1, 2001, pp. 3-21.